


Article

Characterisation of Functional-Trait Dynamics at High Spatial Resolution in a Mediterranean Forest from Sentinel-2 and Ground-Truth Data

Santiago Schauman^{1,2,*}, Alexandre Verger^{2,3}, Iolanda Filella^{2,3} and Josep Peñuelas^{2,3} 

¹ Grupo de Estudios Ambientales, IMASL, Universidad Nacional de San Luis & CONICET, San Luis D5700HHW, Argentina

² CSIC, Global Ecology Unit CREAM-CSIC-UAB, 08193 Bellaterra, Catalonia, Spain; verger@creaf.uab.cat (A.V.); iola@creaf.uab.cat (I.F.); josep.penuelas@uab.cat (J.P.)

³ CREAM, 08193 Cerdanyola del Vallès, Catalonia, Spain

* Correspondence: santischauman@gmail.com; Tel.: +54-266-452-0300

Received: 17 October 2018; Accepted: 17 November 2018; Published: 23 November 2018



Abstract: The characterisation of functional-trait dynamics of vegetation from remotely sensed data complements the structural characterisation of ecosystems. In this study we characterised for the first time the spatial heterogeneity of the intra-annual dynamics of the fraction of absorbed photosynthetically active radiation (FAPAR) as a functional trait of the vegetation in Prades Mediterranean forest in Catalonia, Spain. FAPAR was derived from the Multispectral Instrument (MSI) on the Sentinel-2 satellite and validated by comparison with the ground measurements acquired in June 2017 at the annual peak of vegetation activity. The validation results showed that most of points were distributed along the 1:1 line, with no bias nor scattering: $R^2 = 0.93$, $p < 0.05$; with a root mean square error of 0.03 FAPAR (4.3%). We classified the study area into nine vegetation groups with different dynamics of FAPAR using a methodology that is objective and repeatable over time. This functional classification based on the annual magnitude (FAPAR-M) and the seasonality (FAPAR-CV) from the data on one year (2016–2017) complements structural classifications. The internal heterogeneity of the FAPAR dynamics in each land-cover type is attributed to the environmental and to the specific species composition variability. A spatial autoregressive (SAR) model for the main type of land cover, evergreen holm oak forest (*Quercus ilex*), indicated that topographic aspect, slope, height, and the topographic aspect x slope interaction accounted for most of the spatial heterogeneity of the functional trait FAPAR-M, thus improving our understanding of the explanatory factors of the annual absorption of photosynthetically active radiation by the vegetation canopy for this ecosystem.

Keywords: Sentinel-2; field campaign; validation; mediterranean forest; functional-trait dynamics; spatial heterogeneity

1. Introduction

Characterisation of the dynamics of vegetation functional traits complements structural characterisation of ecosystems [1]. These characterisations are of special interest in ecological studies of climate change, because functional traits tend to respond faster than structural traits to environmental changes [2,3].

The dynamics of functional traits of vegetation can be assessed using various synthetic variables of the annual activity (e.g., annual magnitude and seasonality) derived from remote sensing data at different spatial and temporal scales [1,3–11]. Time series of satellite data are particularly useful

for studying the temporal dynamics of the fraction of absorbed photosynthetically active radiation (FAPAR). The FAPAR corresponds to the fraction of photosynthetically active radiation (radiation at wavelengths of 0.4–0.7 μm) absorbed by the canopy. It depends on canopy structure, vegetation element optical properties and illumination conditions. FAPAR is one of the main components of primary productivity models [12]. It is a key variable for monitoring vegetation, studying the carbon cycle, and modelling climate. FAPAR has been recognized as an essential climate variable by the Global Climate Observing System (GCOS) [13].

The Multispectral Instrument (MSI) on the Sentinel-2 (S2) satellite (<https://earth.esa.int/web/sentinel>) provides data with a high frequency of acquisition (5 days after S2A and S2B are in tandem and 10 days when only S2A was on orbit) and a high spatial resolution (10 m, 20 m or 60 m depending on the spectral band), which are adequate for the characterisation of the functional-trait dynamics of vegetation cover at a high level of detail. FAPAR can be processed on demand using the Sentinel-2 data service platform (<https://s2.boku.eodc.eu>) [14], which provides atmospherically corrected images and biophysical variables, including FAPAR, for any land surface on Earth.

Validation exercises are essential in remote-sensing studies for assessing the uncertainty associated to the satellite products. We directly validated the Sentinel-2 satellite products at our study site by comparison with ground-truth measurements [15,16]. Ground measurements acquisition and sampling design follow the international protocols of best practices standards for the validation of satellite products of the Committee on Earth Observation Satellites (CEOS) Working Group on Calibration and Validation (WGCV), Land Product Validation (LPV) subgroup [17], which are regularly applied to validate vegetation products generated by the Copernicus Land Monitoring Service [18].

Objectives

The main objective of this study was to characterise the spatial heterogeneity of FAPAR dynamics as a functional trait of a Mediterranean forest in Prades, Catalonia, using remote-sensing techniques and in situ measurements.

The specific objectives were to:

- I validate a high-spatial-resolution FAPAR product generated from the MSI data for a representative area of Prades forest with ground-truth measurements;
- II characterise the intra-annual FAPAR activity with two synthetic variables derived from FAPAR seasonal curves: annual magnitude (FAPAR-M) and seasonality (FAPAR-CV);
- III analyse the relationship between the topographic variables and the spatial heterogeneity of FAPAR-M of the main type of land cover at the study site: evergreen oak forest (*Quercus ilex*).

2. Materials and Methods

The study site is first described (Section 2.1). Then the databases (Section 2.2) and methods (Sections 2.3–2.5) are presented. Figure 1 shows a flow chart of the methodology.

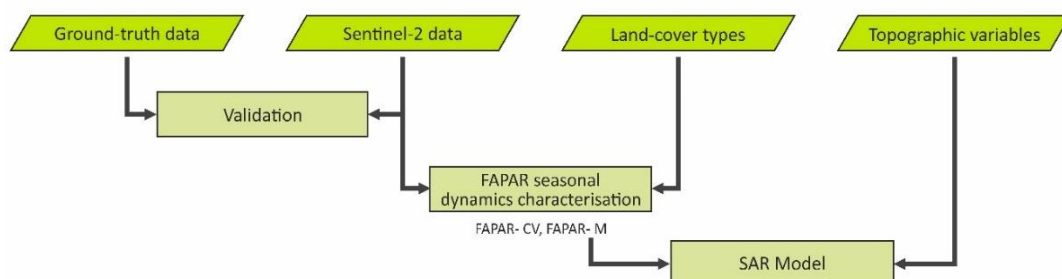


Figure 1. Flow chart of the methodology.

2.1. Study Site

The study was conducted at a site 3.5×3.5 km in a Mediterranean forest (coordinates of the centre in the WGS84 geographic coordinate system: $41^{\circ}20'26.76''\text{N}$, $1^{\circ}2'16.77''\text{E}$) in Prades, Tarragona, Catalonia, Spain, in a mountainous area with altitudes ranging between 622 and 1138 m a.s.l. We defined the study area taking into account the representativeness of natural conditions of the forest and minimising anthropic environments. The main land-cover types at the study site are evergreen oak forest (*Q. ilex*), Scots pine forest (*Pinus sylvestris*), Austrian pine forest (*P. nigra*), and Pubescent oak forest (*Q. pubescens*) (Figure 2). Climatic conditions are typical of montane Mediterranean climates. The mean annual temperature is 12°C and average annual rainfall is 658 mm. Summer drought lasts from mid-June to mid-September [19]. The mean annual temperature for the study period (15 October 2016 to 15 October 2017) was 15°C , and the total cumulative rainfall was 600 mm, calculated using data from the State Meteorological Agency (AEMET) [20].

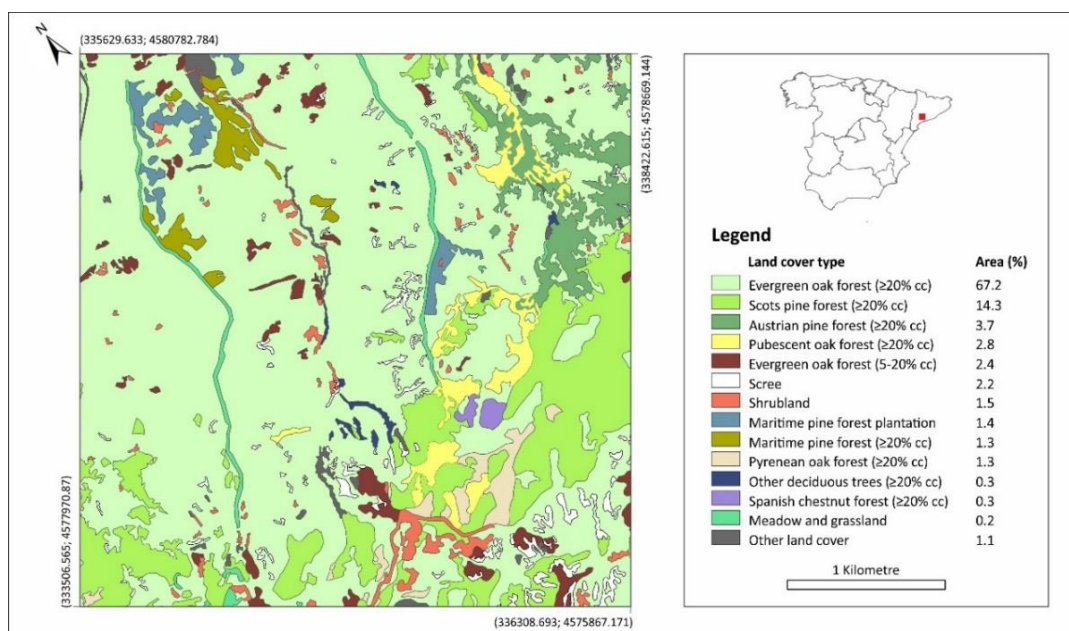


Figure 2. Types and canopy coverages (cc) of the land covers in the study site. The percentage of the area of each land cover type over the entire study site is shown in detail. Data obtained from the Land Cover Map of Catalonia [21]. Reference System ETRS89 Universal Transverse Mercator (UTM) zone 31 N.

2.2. Databases

2.2.1. Satellite Products

We used time series of FAPAR derived from MSI data on board Sentinel-2 (<https://earth.esa.int/web/sentinel>). The FAPAR was processed on demand by the Sentinel-2 data service platform on the Earth Observation Data Centre (EODC) (<https://s2.boku.eodc.eu>) [14]. The platform processes European Space Agency's (ESA) Level-1C top-of-atmosphere reflectance using the Sen2Cor algorithm (version 2.4) to obtain atmospherically-corrected bottom-of-atmosphere (BoA) reflectance (Level-2A). The FAPAR products were generated using a neural network algorithm [22] calibrated on simulations from the coupled PROSPECT and SAIL radiative transfer models. The instantaneous FAPAR value at the time of the satellite overpass is computed directly from the radiative transfer model in the green parts of the canopy. The FAPAR products have a spatial resolution of 10 m and a temporal resolution of 10 d (5 d after the launch of the second twin satellite Sentinel-2). We checked the spatial accuracy

of Sentinel-2 products using ground control points (GPS coordinates of bare soil areas, roads, and firebreaks), and we did not identify geolocation problems for our study site.

We identified and distinguished between cloud-free satellite products for one year (15 October 2016 to 15 October 2017) by visual interpretation of Sentinel-2 atmospherically corrected BoA reflectance (Level-2A) data. We generated true- and false-colour RGB images for each date to identify the shape, size, pattern, tone, texture, shadowing, and association of the elements. We evaluated all images available for the study period, ultimately selecting a total of 19 products for the construction of the seasonal curves.

2.2.2. Topographic Variables

We used a digital elevation model (DEM) with high spatial resolution (pixel size of 10 m) provided by the Data Services Platform for Sentinel-2 (<http://s2.boku.eodc.eu/>). We obtained the variable height and derived the variables slope, soil water distribution, topographic position and aspect for the main type of land cover in the study site (evergreen oak forest, *Q. ilex*) (Figure 3).

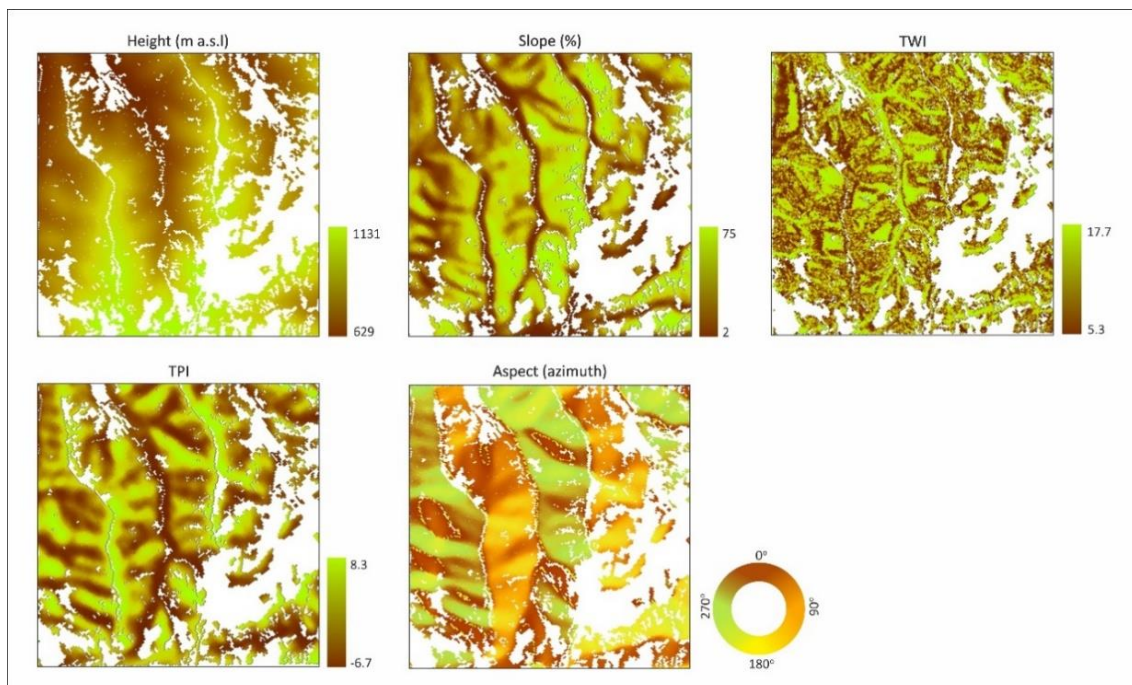


Figure 3. Topographic variables obtained and derived from the digital elevation model (DEM) for the main vegetation cover type at the study site (evergreen oak forest, *Quercus ilex*): height (metres above sea level), slope (in percentage), Topographic Wetness Index (TWI), Topographic Position Index (TPI) and topographic aspect (azimuth that slopes are facing: 0° north, 90° east, 180° south, 270° west).

The soil water distribution, which is affected by topography, was calculated using the Topographic Wetness Index (TWI) [23], determined as:

$$TWI = \ln (a / \tan \beta),$$

where a is the area of a specific catchment, the local upslope area draining through a certain point per unit contour length, and β is the local slope. TWI was calculated using the Multiple Flow Direction algorithm based on maximum downslope gradient (MFD-md) [24,25], available in the System for Automated Geoscientific Analyses (SAGA 2.3.2) programme.

The topographic position of the terrain was calculated using the Topographic Position Index (TPI), defined as the difference in height (positive or negative) between a central pixel and its

surrounding cells within a predetermined radius (landscape unit considered) [26,27]. We predefined a landscape unit radius of 150 m to highlight minor valleys and ridges by the visual interpretation of very-high-spatial-resolution (VHR) satellite imagery using Google Earth.

2.2.3. Land-Cover Types

The main land-cover types at the study site (Figure 2) were analysed by the high-resolution thematic cartography of the Land Cover Map of Catalonia and ground measurements. Appendix A provides further details and descriptions of the main land-cover types in the study area.

We characterised the intra-annual dynamics of FAPAR by type of land cover using the shapefile for the Land Cover Map of Catalonia (level 5 of the legend) [21] and calculated the areas using the ETRS89 UTM zone 31 N reference system.

2.3. Validation of Satellite Products

2.3.1. Ground Measurements and Data Processing

The satellite products (see Section 2.2.1) were validated following the international protocols of best practices standards of the CEOS WGCV LPV subgroup [17].

Ground-truth data were acquired using digital hemispherical photography (DHP), which allowed the calculation of FAPAR, and other variables of canopy architecture (e.g., Leaf Area Index (LAI), Fraction of green vegetation cover (FCOVER)), based on directional measurements of the fraction of gaps in the vegetation cover [28–32]. We used a digital Nikon camera and an extreme wide-angle lens (180° fisheye lens) for each measurement.

We used CAN-EYE v6.4 software (<https://www6.paca.inra.fr/can-eye>) for processing the RGB hemispherical photographs and extracting the FAPAR canopy values. We defined the characteristics of the camera + fisheye lens system (optical centre at the centre of the image, equidistant projection function) and all information required for the software [33] for the processing. We also masked the field of view of the lens to values within the range 0–60° to ensure that the area captured was within the sampling unit. The software allowed us to extract the FAPAR value for each sampling point of the study site by a supervised-classification process using the green elements of the RGB digital images. The CAN-EYE FAPAR values [33,34], corresponded to the direct instantaneous FAPAR, “Black Sky FAPAR”, obtained from the fraction of intercepted photosynthetically active radiation as 1-gap fraction at solar zenith corresponding to 10:30 (Sentinel-2 revisit time for the study site: 10:50) (<https://sentinel.esa.int/web/sentinel/missions/sentinel-2/acquisition-plans>).

We acquired two sets of hemispherical photographs for sampling units with over and understory: upward looking (overstory) and downward looking (understory). The two sets of acquisitions were processed separately to derive FAPAR [16,35]. FAPAR was calculated assuming the independence of the gaps inside the understory and inside the overstory. The biophysical variable was calculated as:

$$\text{FAPAR} = 1 - (1 - \text{FAPAR overstory}) * (1 - \text{FAPAR understory})$$

2.3.2. Sampling Scheme

We designed the sampling scheme following the recommendations for running a field campaign of the FP7 ImagineS project (<http://fp7-imagines.eu>), consistent with the Validation of Land European Remote sensing Instruments (VALERI) project (<http://w3.avignon.inra.fr/valeri/>) [15].

We first surveyed the study area to identify the types of vegetation cover, determine the accessibility of the terrain, and plan the logistics of collecting the field data. We then programmed the date for the ground measurements to 15 June 2017 taking into account: (a) the period of maximum vegetation greenness for the study site (analysed with time series of the Normalized Difference Vegetation Index (NDVI)) to minimise problems due to the presence of non-green vegetation

elements [15], (b) the acquisition plans for Sentinel-2 (<https://sentinel.esa.int/web/sentinel/missions/sentinel-2/acquisition-plans>), and (c) the weather forecast, increasing the probability for clear skies.

The elementary sampling unit (ESU) consisted of a 10×10 m plot to match the pixel size of the Sentinel-2 satellite biophysical product to be validated. We acquired 8–15 measurements (DHP) for each ESU to obtain a reasonable estimate of the gap fraction [29,33]. We followed a predefined sampling scheme to locate the photos within the ESU as independently as possible (Figure 4).

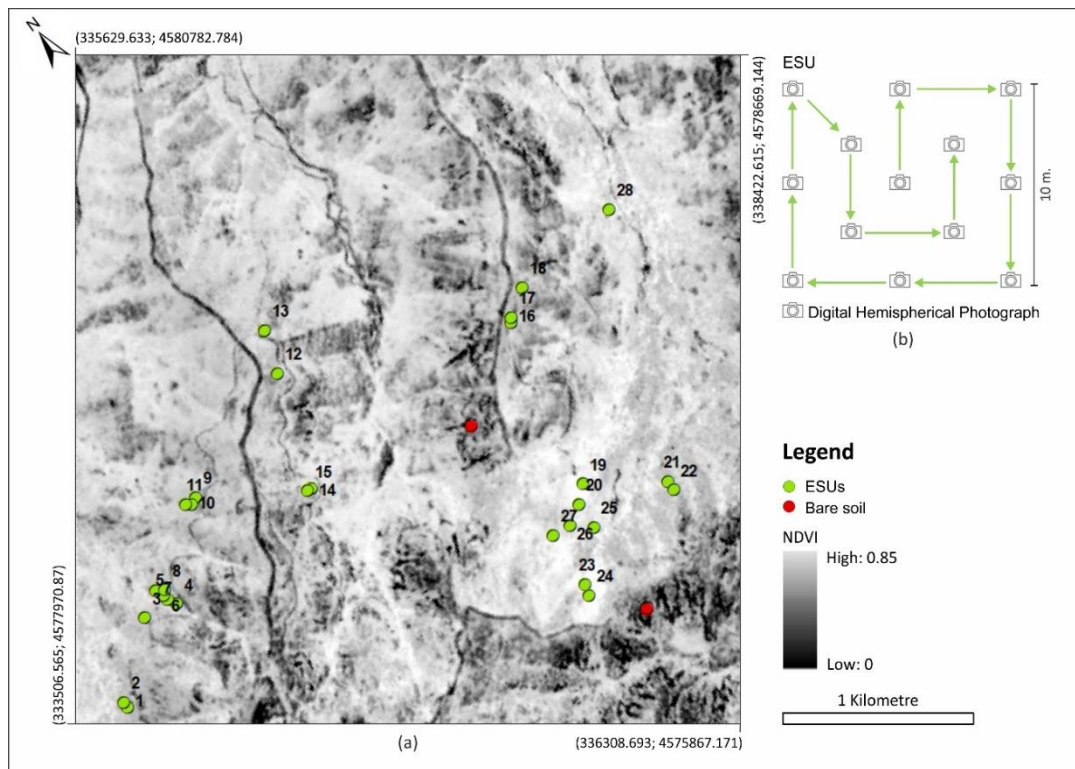


Figure 4. (a) Normalized Difference Vegetation Index (NDVI) cartography for the study area (satellite imagery acquired on 12 June 2017) indicating the location of the 28 elementary sampling units (ESUs) and the two additional units of bare soil. Reference System ETRS89 UTM zone 31 N. (b) The sampling scheme of the measurements within an ESU is shown in detail, where arrows indicate the path followed during the sampling.

We installed 28 ESUs for six forest classes to represent the main vegetation cover types and FAPAR values at the study site (Figure 4). We established the ESUs at distances higher than 50 m from the borders of roads and surrounded by pixels with the same type of vegetation, because the radiative transfer of a single pixel may be influenced by the neighbouring pixels by lateral fluxes [36]. The centre of each ESU was geolocated using a global positioning system receiver.

Although our sampling took into account the main land covers and the environmental heterogeneity of the site, only a fraction of the FAPAR range of the study site (Figure 5) was finally represented by the ESUs due to the difficulty of accessing the terrain. The FAPAR values sampled in situ were mostly between 0.58 and 0.90 (range 0.32), with a mean of 0.69 and coefficient of variation of 13%. Most of the ESUs were evergreen oak forest (15 of the 28 sampling units), followed by Scots pine (5), Maritime pine (3), Pyrenean oak (2), Spanish chestnut (2), and Pubescent oak (1) forests (Figure 5). Finally, due to the lack of ESUs with FAPAR values lower than 0.58, we indirectly geolocated by visual interpretation of VHR satellite imagery using Google Earth two additional units of bare soil where we assume zero values for FAPAR. Appendix B provides further details of the ESU geolocation and FAPAR values.

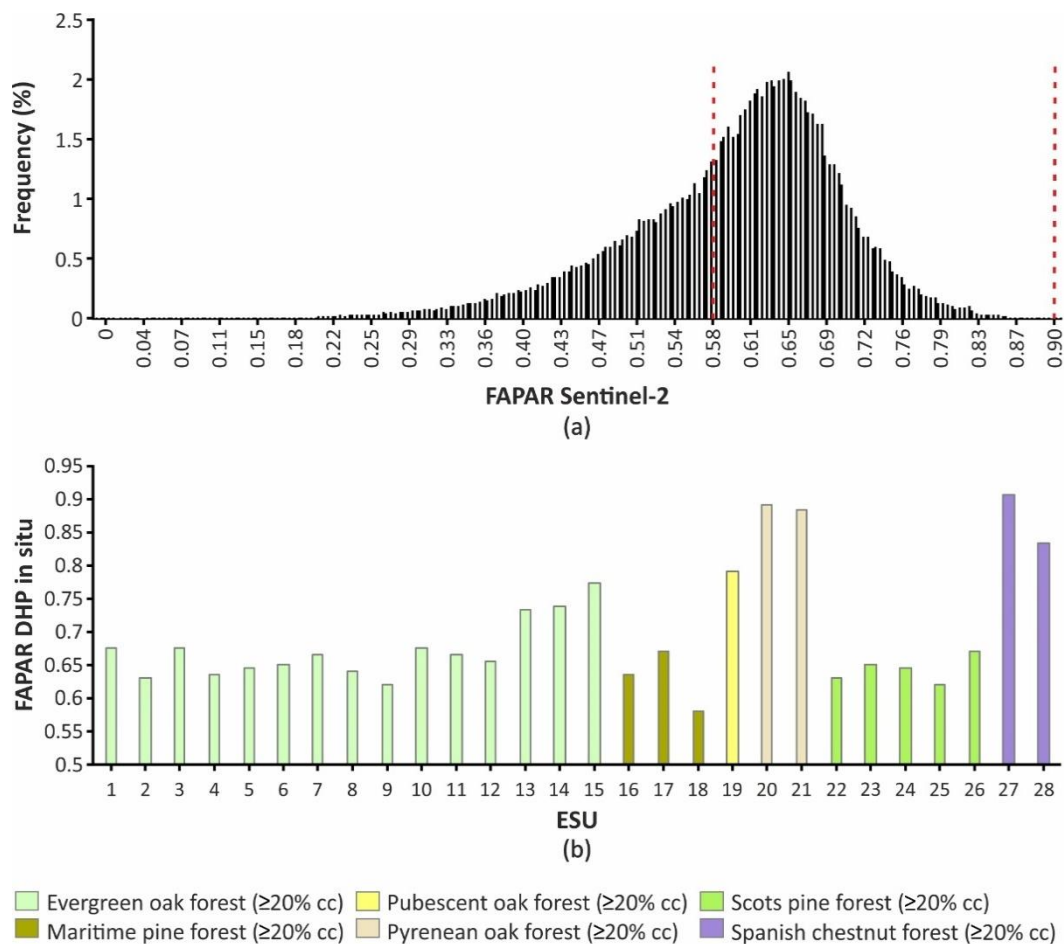


Figure 5. (a) Frequency distribution of the fraction of absorbed photosynthetically active radiation (FAPAR) from Sentinel-2 satellite images for the study site and sampling period (three days between satellite acquisition and the ground measurements). The red dotted line indicates the FAPAR range sampled in situ. (b) FAPAR ground measurements obtained from digital hemispherical photography (DHP) for each elementary sampling unit (ESU) by type and canopy coverage (cc) of land cover.

2.3.3. Validation

We performed linear regressions to estimate the strength of the relationship between the ground-truth FAPAR values and the Sentinel-2 FAPAR product values. We assume no temporal variation in FAPAR within the three days between satellite acquisition on 12 June and the ground measurements on 15 June. We compared the slope and intercept with the 1:1 line [37]. We also calculated the root mean square error (RMSE) to represent the standard deviation of the differences between the values of the Sentinel-2 FAPAR product and ground-truth FAPAR to complement the validation. RMSE was calculated as:

$$\text{RMSE} = \sqrt{\frac{\sum_{i=1}^n (X_{in\ situ,i} - X_{sentinel2,i})^2}{n}}$$

where $X_{in\ situ}$ is the ground-truth FAPAR value and $X_{sentinel2}$ is the Sentinel-2 FAPAR product value.

2.4. Analysis and Characterisation of Functional-Trait Dynamics

We used one-year of cloud-free time series of FAPAR (see Section 2.2.1) to describe, classify, and map the intra-annual functional activity of the vegetation cover considering existing methodologies for functional characterisations of ecosystems [1,4–9,11].

We calculated eight semi-season composites (late autumn, early winter, late winter, early spring, late spring, early summer, late summer, and early autumn) as the average of the satellite data available for each period (Table 1). We performed linear interpolations for late autumn and early winter because of: (i) the lack of cloud-free images for these semi-seasons; and (ii) the detection of contaminated pixels by terrain shadows, due to the lower solar angle in these periods. Linear interpolations were performed between early autumn and late winter values in the QGIS 2.18.14 environment.

Table 1. Cloud-free satellite images for each semi-season composite.

Semi-Season Product	Start	End	Cloud-Free Satellite Images				
Late autumn	6 November	20 December	17 November				
Early winter	21 December	3 February					
Late winter	4 February	20 March	25 February	14 March	17 March		
Early spring	21 March	5 May	3 April	6 April			
Late spring	6 May	20 June	6 May	16 May	26 May	12 June	
Early summer	21 June	4 August	2 July	5 July	4 August		
Late summer	5 August	20 September	11 August	14 August	10 September	13 September	20 September
Early autumn	21 September	5 November	10 October	13 October			

We generated one FAPAR seasonal curve with the semi-season composites for each pixel of the study area (Figure 6) and calculated two synthetic variables from the seasonal curves of FAPAR that capture important traits of the FAPAR dynamics: FAPAR-M as the mean of the eight semi-season composites and FAPAR-CV as the ratio of the standard deviation to the mean.

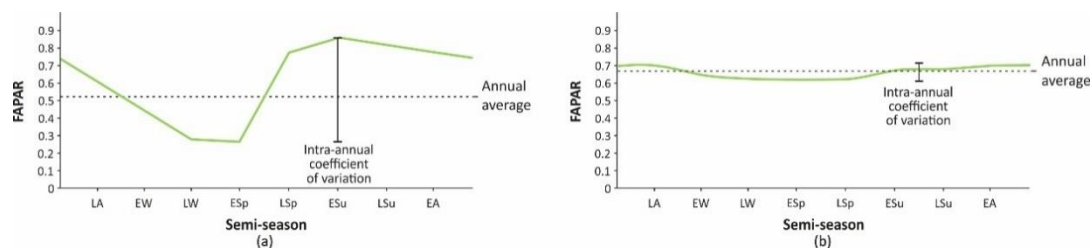


Figure 6. Examples of the seasonal dynamics of the fraction of absorbed photosynthetically active radiation (FAPAR) for two systems with: (a) moderate annual magnitude and high seasonal variability; and (b) high annual magnitude and low seasonal variability. LA, late autumn; EW, early winter; LW, late winter; ES_p, early spring; LSp, late spring; ES_u, early summer; LS_u, late summer; EA, early autumn.

We analysed the spatial heterogeneity of FAPAR-M and FAPAR-CV over the entire study area and per land-cover type (see Section 2.2.3). We identified vegetation groups with different dynamics of FAPAR. The groups were defined using fixed limits between classes to allow future inter-annual comparisons, capturing the year-to-year dynamics [11]. The range of variation of FAPAR-M and FAPAR-CV were divided into three classes (low, medium, and high), fixing intervals at 1/3 of the ranges within 2.5 and 97.5 percentiles of the distributions to avoid long tails in the histograms. The combination of the generated classes (3 × 3) allowed us to identify, in a single map, the pixels for the vegetation groups, based on different dynamics of radiation absorption. We assigned a two-number code to each vegetation group. The first number corresponded to the FAPAR-M class, and the second number corresponded to the FAPAR-CV class. The coding in both cases was 1 for the low class, 2 for the

medium and 3 for the high. We analysed the spatial patterns of the vegetation groups generated and evaluated the correspondence between them and the main vegetation cover types of the study area.

2.5. Explanatory Topographic Factors of FAPAR-M Spatial Variability

We analysed the relationship between the topographic variables (see Section 2.2.2) and the spatial heterogeneity of FAPAR-M for the main land cover class in the study area, that is, evergreen oak forest (*Q. ilex*) using spatial autoregressive (SAR) models.

We compiled a spatially explicit database integrating FAPAR-M as the dependent variable and height (DEM), slope, TWI, TPI, and aspect of the terrain (derived from the DEM) as independent variables. We thus integrated all variables in a geographic information system (GIS). We re-sampled the spatial resolution of the satellite imagery to 50-m cells to minimise the spatial autocorrelation of the data and considered for the models only cells with evergreen oak forest (*Q. ilex*) cover (cells number = 2246). We obtained the average FAPAR-M and the height, slope, TWI, TPI, and aspect of the terrain for each 50-m cell. The topographic aspect data, whose original units were azimuth angles, were transformed into a four-level categorical variable (north, south, east, west). The collinearity of the explanatory topographic factors were inspected using Pearson correlation coefficients and generalised variance-inflation factors (GVIFs) [38,39], using the R 'car' package [40]. Appendix C provides further details of the collinearity analysis.

All models were fitted using the R 'spdep' package and the lagsarlm function [41], with the queen criterion on the matrix of spatial weights [42]. The normality, linearity, and homoscedasticity of the residuals were inspected visually. We applied model selection to include those terms that minimised the value of the Akaike Information Criterion (AIC) [43]. Statistical analysis was performed in R 3.4.2.

3. Results

3.1. Validation of Satellite Products

The validation results (Figure 7) showed that the Sentinel-2 FAPAR product at the study site agreed well with the ground-truth data ($n = 28$) with an RMSE of 0.03 (4.3% of the mean), and RMSE of 0.031 (4.8% of the mean) with the two additional bare soil sampling units ($n = 30$). The data points were distributed along the 1:1 line, with no bias or scattering. The coefficients of the regression were close to one: $R^2 = 0.93$ ($p < 0.05$) for the $n = 28$ ESUs, and $R^2 = 0.98$ ($p < 0.05$) including the two additional sampling units ($n = 30$).

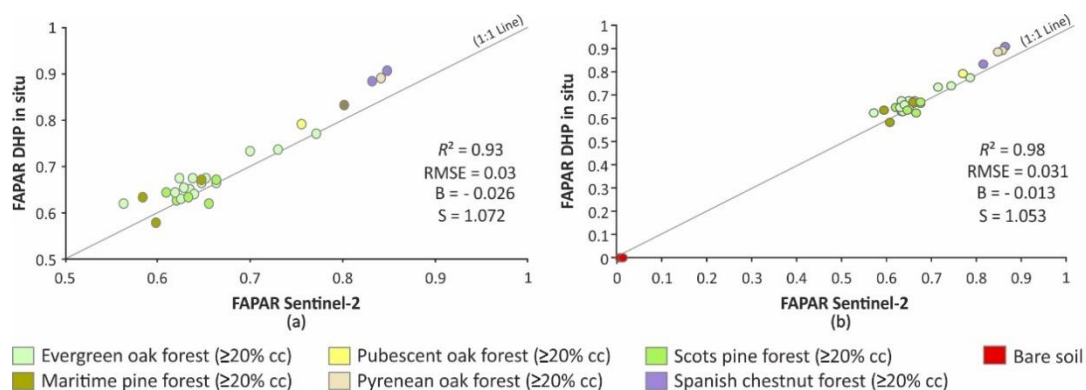


Figure 7. Scatter-plots between ground measurements obtained from digital hemispherical photography (DHP) and the corresponding fraction of absorbed photosynthetically active radiation (FAPAR) from Sentinel-2 satellite images. FAPAR ground measurements for each elementary sampling unit by type and canopy coverage (cc) of land cover is shown in detail. (a) Only ground-truth elementary sampling unit data ($n = 28$), (b) with the extra units of bare soil obtained from very-high-resolution satellite imagery ($n = 30$).

3.2. Analysis and Characterisation of Functional-Trait Dynamics

FAPAR-M had a mean of 0.61 and a spatial standard deviation of 0.09. FAPAR-M ranged between 0.05 and 0.86 (range 0.81), with a negatively skewed distribution (Figure 8), where the values between 0.63 and 0.67 were the most frequent. Values were extreme for rocky outcrops and deciduous trees other than those of our land-cover types ($\geq 20\%$ canopy coverage (cc)), respectively.

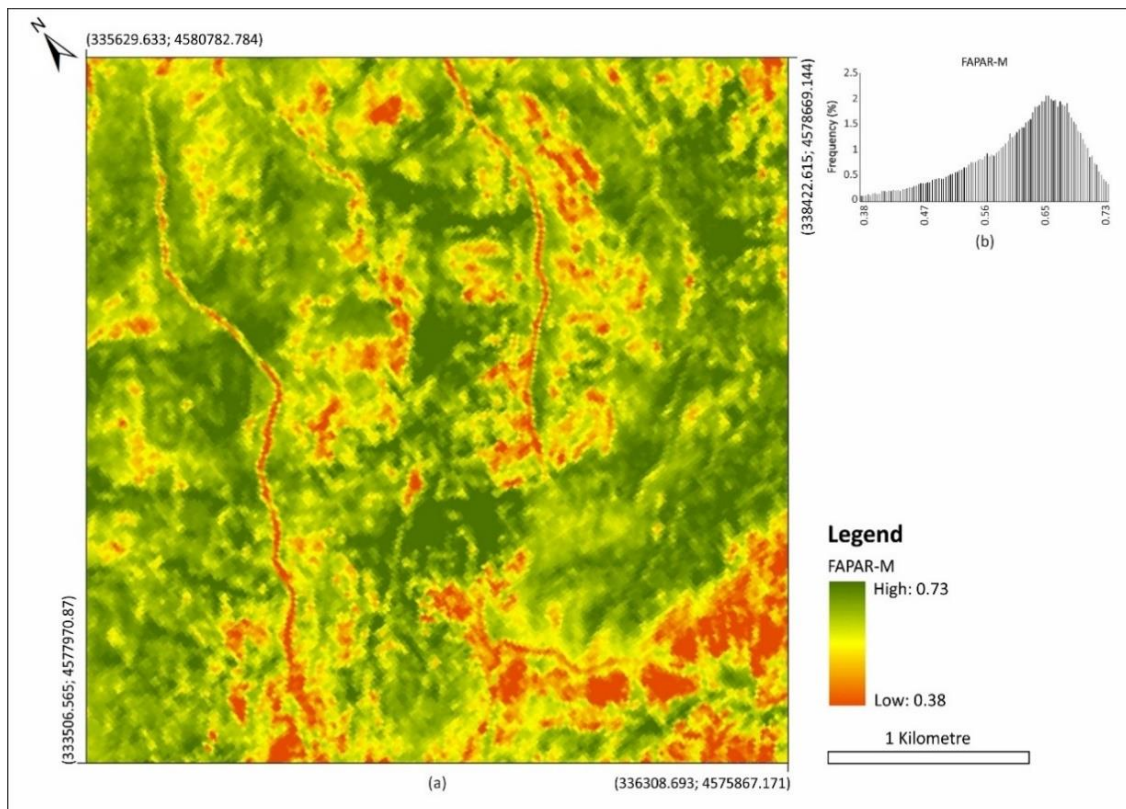


Figure 8. (a) Geographically explicit data set for the annual magnitude of the fraction of absorbed photosynthetically active radiation (FAPAR-M), derived from the seasonal curves of FAPAR obtained with one year of data (2016/2017) from the Multispectral Instrument (MSI) on the Sentinel-2 satellite. Reference System ETRS89 UTM zone 31 N. (b) Negatively skewed frequency distribution of FAPAR-M between the 2.5 (0.38) and 97.5 (0.73) percentiles.

The geographically explicit data set for FAPAR-M allowed observation of the spatial distribution of the data range (Figure 8), which identified specific contrasting patterns in the pixel groupings across the study site.

FAPAR-CV at the study site had a mean of 0.06 and a spatial standard deviation of 0.04. FAPAR-CV ranged between 0.01 and 0.72 (range 0.71), with a positively skewed distribution (Figure 9), where the values between 0.03 and 0.04 were the most frequent. Values were extreme for Maritime pine forest ($\geq 20\%$ cc) and Pyrenean oak forest ($\geq 20\%$ cc), respectively.

The geographically explicit data set for FAPAR-CV allowed observation of the spatial distribution of the data range (Figure 9), which identified specific contrasting patterns in the pixel groupings across the study site, as with FAPAR-M.

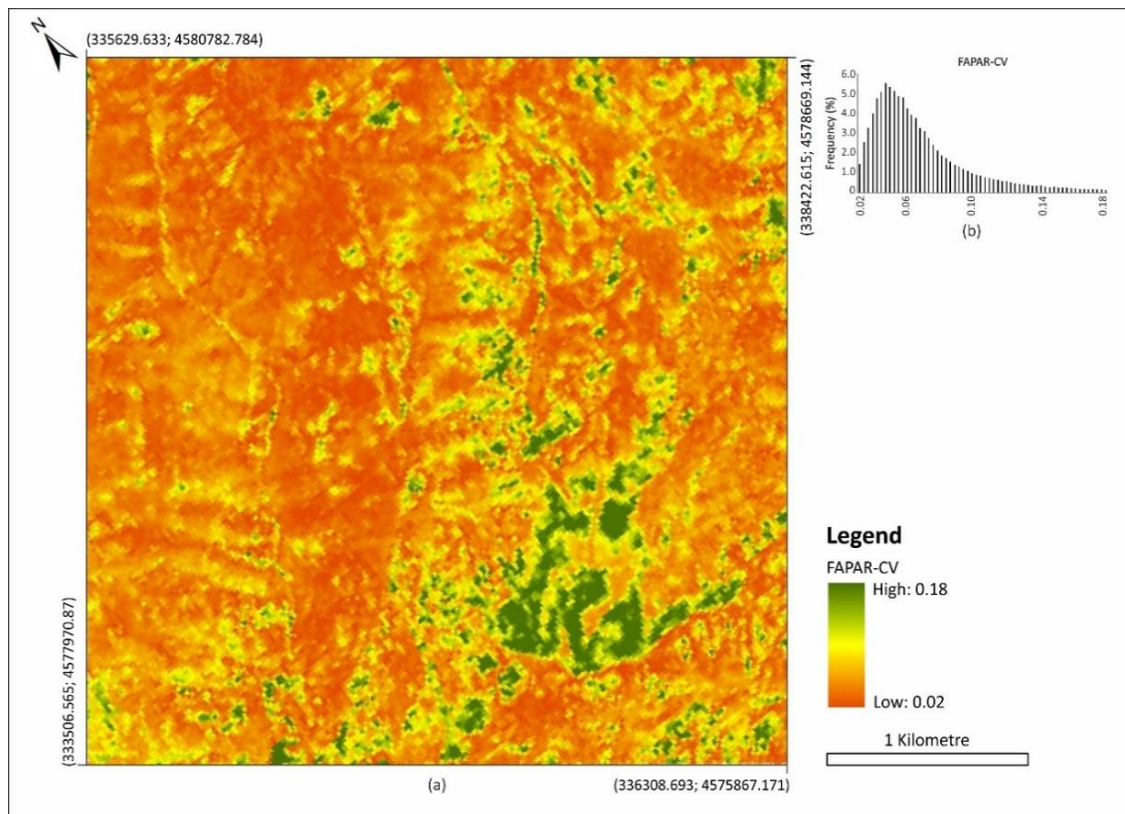


Figure 9. (a) Geographically explicit data set for the seasonality of the fraction of absorbed photosynthetically active radiation (FAPAR-CV), derived from the seasonal curves of FAPAR obtained with one year of data (2016/2017) from the Multispectral Instrument on the Sentinel-2 satellite. Reference System ETRS89 UTM zone 31 N. (b) Positively skewed frequency distribution of FAPAR-CV between the 2.5 (0.02) and 97.5 (0.18) percentiles.

The integration of the FAPAR seasonal curves from the geographically explicit data set with data from the Land Cover Map of Catalonia allowed us to analyse the FAPAR intra-annual dynamics of the main types of land cover (Figure 10).

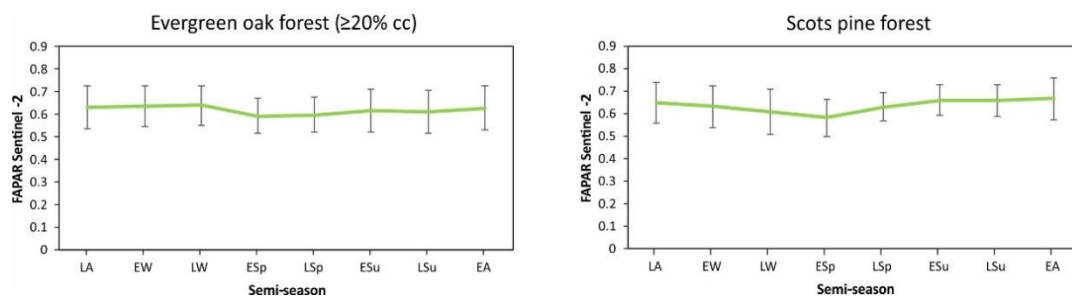


Figure 10. Cont.

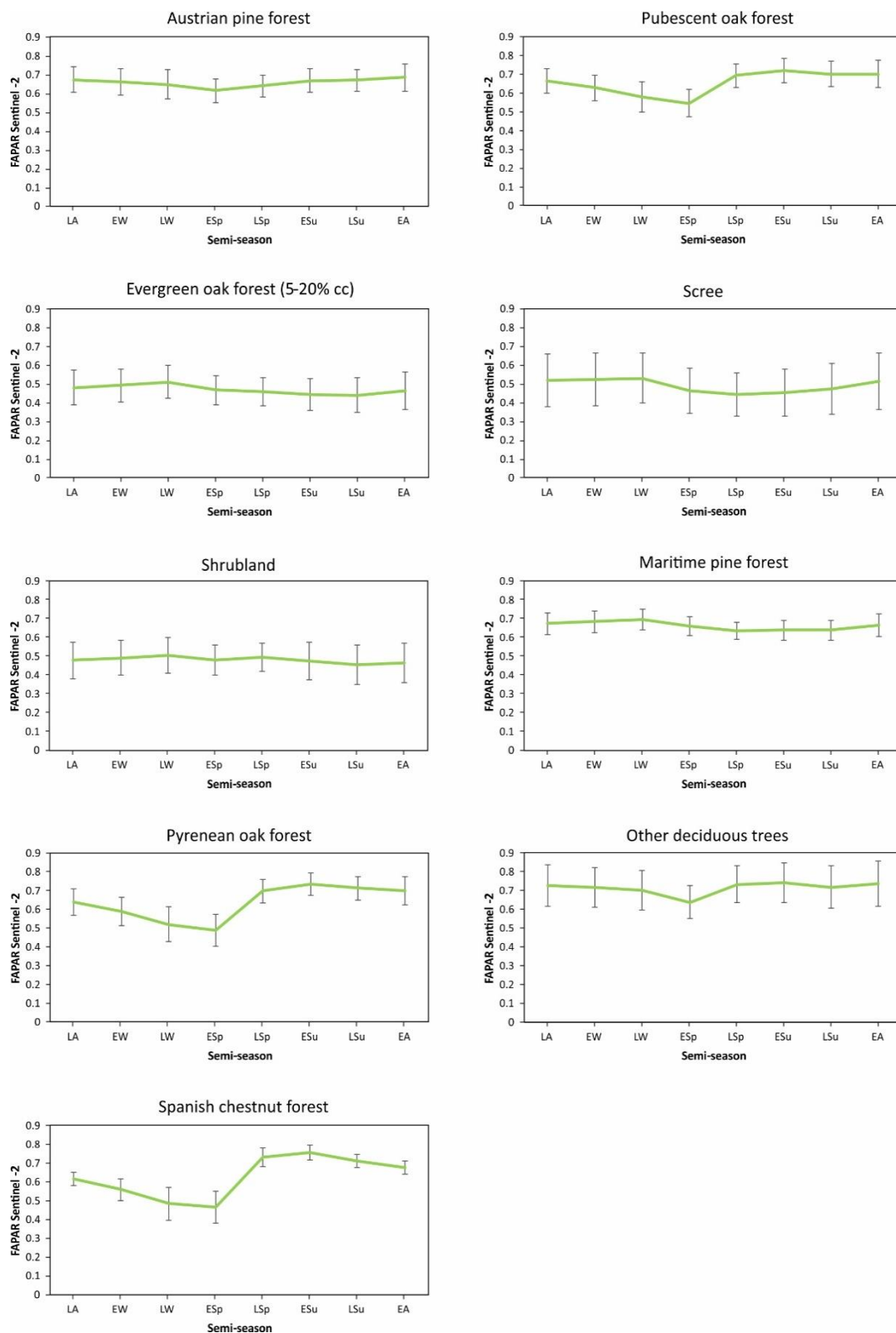


Figure 10. Seasonal curves of the fraction of absorbed photosynthetically active radiation (FAPAR) for the main types and canopy coverages (cc) of land cover, obtained from one year of data (2016/2017) from the Multispectral Instrument on the Sentinel-2 satellite and the Land Cover Map of Catalonia. The error bars indicate the spatial standard deviation. LA, late autumn; EW, early winter; LW, late winter; ESu, early spring; LSp, late spring; ESu, early summer; LSu, late summer; EA, early autumn.

The main type of land cover, evergreen oak forest ($\geq 20\%$ cc), had a moderate FAPAR-M (mean = 0.619), with a spatial heterogeneity (calculated using the spatial standard deviation) of 0.085 (13.7% of the mean). Other deciduous trees had the highest FAPAR-M (mean = 0.715), and evergreen oak forest (5–20% cc), shrubland, and scree had the lowest values (mean FAPAR-M = 0.47, 0.48, 0.489, respectively). The remaining types of land cover had intermediate values of FAPAR-M (Figure 11). The spatial heterogeneity of FAPAR-M was highest for scree, shrubland, and evergreen oak forest (5–20% cc), with spatial standard deviations of 0.13, 0.09, and 0.08 and means of 26, 18, and 18%, respectively. The other types of land cover had spatial heterogeneities ranging from moderate to low (Figure 11).

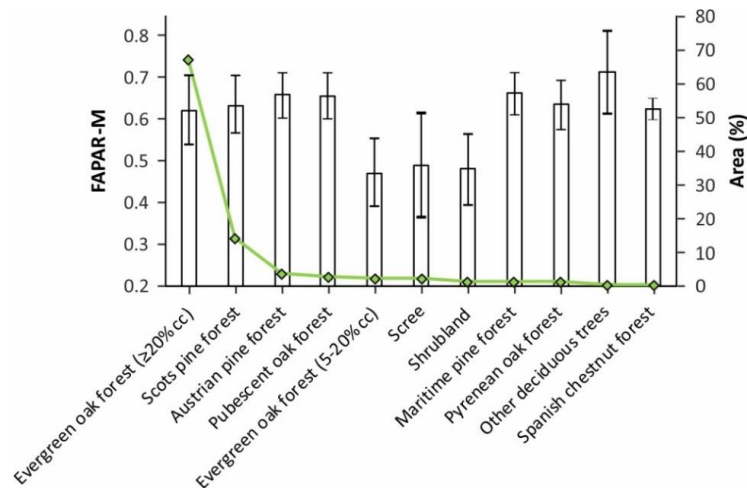


Figure 11. Annual magnitude of the fraction of absorbed photosynthetically active radiation (FAPAR-M) for the main types and canopy coverages (cc) of land cover. The bars correspond to mean FAPAR-M, and the error bars correspond to the spatial standard deviation. The green line corresponds to the percentage of the area of each cover type over the entire study site (see Section 2.1).

Evergreen oak forest ($\geq 20\%$ cc) had the second lowest intra-annual temporal variability (mean FAPAR-CV = 0.052), with a spatial heterogeneity (calculated using the spatial standard deviation) of 0.03 (mean = 56.5%). Pyrenean oak forest had the highest seasonal variability (mean FAPAR-CV = 0.154), and Maritime pine forest had the lowest (mean FAPAR-CV = 0.041). FAPAR-CV had higher values of spatial heterogeneity than FAPAR-M for all the types of land cover (Figure 12).

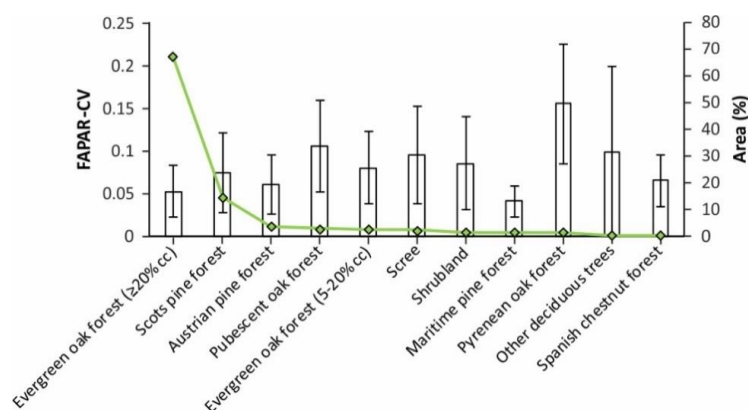


Figure 12. Seasonality of the fraction of absorbed photosynthetically active radiation (FAPAR-CV) for the main types and canopy coverages (cc) of land cover. The bars correspond to mean FAPAR-CV, and the error bars correspond to the spatial standard deviation. The green line corresponds to the percentage of the area of each cover type over the entire study site (see Section 2.1).

The categorisation of the gradients of FAPAR-M and FAPAR-CV and their subsequent combination allowed us to identify nine vegetation groups with different dynamics of absorption of photosynthetically active radiation (Figure 13). The map shows the most frequent patterns of the FAPAR intra-annual dynamics for the study site (2016–2017): low seasonality with medium and high magnitudes of annual FAPAR (group codes 2-1 and 3-1, respectively). The map highlights the clear and contrasting patterns across the study site, although the remaining groups had lower percentages of occupation (Table 2).

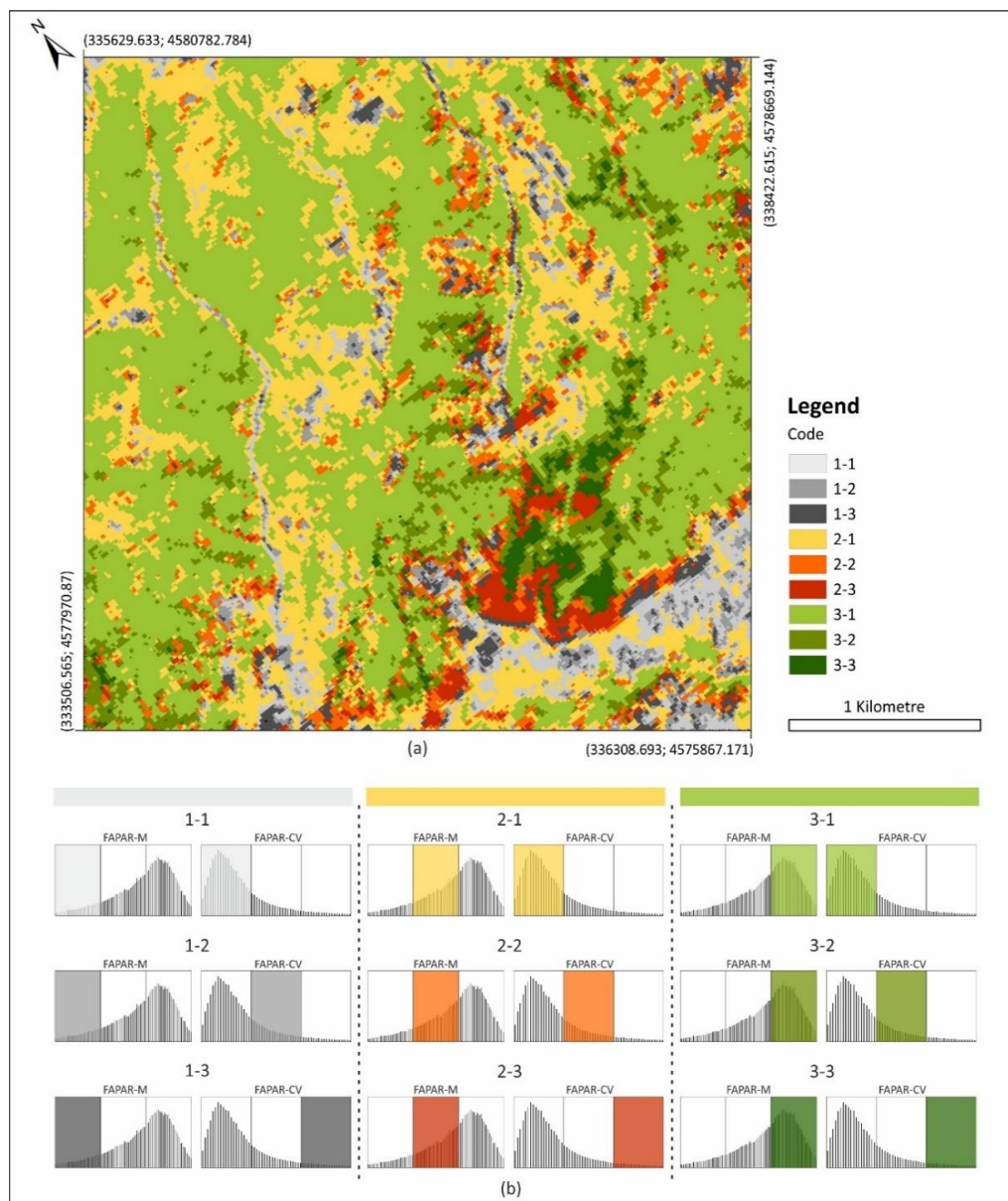


Figure 13. (a) Map of the vegetation groups with different dynamics of absorption of photosynthetically active radiation for 2016–2017 obtained from the seasonal curves of the Sentinel-2 satellite data. Reference System ETRS89 UTM zone 31 N. (b) Each group is defined by a two-number code. The first and second numbers (1 = low, 2 = medium, 3 = high) indicate the magnitude and seasonality of the fraction of absorbed photosynthetically active radiation, respectively.

Finally, we evaluated the correspondence between the vegetation groups with different dynamics of absorption of photosynthetically active radiation and the land-cover types across the study site

(Table 3). This analysis did not evaluate the classification of functional-trait dynamics, but objectively evaluated the degree of correspondence with the structural classification for descriptive purposes.

Table 2. Areas of the vegetation groups with different dynamics of absorption of photosynthetically active radiation for 2016–2017.

Group Code	Area (ha)	Area (%)
1-1	60.00	4.90
1-2	52.32	4.27
1-3	32.67	2.67
2-1	278.24	22.71
2-2	80.34	6.56
2-3	36.24	2.96
3-1	567.96	46.36
3-2	92.55	7.56
3-3	24.67	2.01

Table 3. Correspondence between the vegetation groups with different dynamics of absorption of photosynthetically active radiation and the land-cover types across the study site.

Group Code	Land-Cover Type (Canopy Coverage)	Area (ha) (% area)	Correspondence (%)
1-1	Evergreen oak forest ($\geq 20\%$)	36.1 (4.4)	60
	Evergreen oak forest (5–20%)	6.6 (22.5)	11
	Scree	5.1 (19.1)	8
	Shrubland	4.5 (24.6)	7
	Other		14
1-2	Evergreen oak forest ($\geq 20\%$)	26 (3.2)	50
	Evergreen oak forest (5–20%)	7.9 (26.9)	15
	Scree	5.4 (20.2)	10
	Shrubland	5 (27.4)	10
	Other		15
1-3	Evergreen oak forest ($\geq 20\%$)	10.7 (1.3)	33
	Scots pine forest ($\geq 20\%$)	5.9 (3.4)	18
	Shrubland	4.4 (24.1)	13
	Scree	4 (15.0)	12
	Evergreen oak forest (5–20%)	3.6 (12.3)	11
	Other		13
2-1	Evergreen oak forest ($\geq 20\%$)	222.7 (27.4)	80
	Scots pine forest ($\geq 20\%$)	20.6 (11.7)	7
	Other		13
2-2	Evergreen oak forest ($\geq 20\%$)	49.8 (6.1)	62
	Scots pine forest ($\geq 20\%$)	15 (8.5)	19
	Other		19
2-3	Scots pine forest ($\geq 20\%$)	12.2 (6.9)	34
	Evergreen oak forest ($\geq 20\%$)	8.5 (1.0)	23
	Pyrenean oak forest ($\geq 20\%$)	5.2 (32.1)	14
	Pubescent oak forest ($\geq 20\%$)	3.4 (10.1)	9
	Scree	2.3 (8.6)	6
	Other		14
3-1	Evergreen oak forest ($\geq 20\%$)	408.9 (50.3)	72
	Scots pine forest ($\geq 20\%$)	89.4 (50.9)	16
	Austrian pine forest ($\geq 20\%$)	29.5 (65.2)	5
	Other		7
3-2	Evergreen oak forest ($\geq 20\%$)	46.6 (5.7)	50
	Scots pine forest ($\geq 20\%$)	20.9 (11.9)	23
	Pubescent oak forest ($\geq 20\%$)	10.2 (30.3)	11
	Austrian pine forest ($\geq 20\%$)	6.4 (14.2)	7
	Other		9
3-3	Pubescent oak forest ($\geq 20\%$)	8 (23.7)	33
	Pyrenean oak forest ($\geq 20\%$)	5.1 (31.5)	21
	Evergreen oak forest ($\geq 20\%$)	2.5 (0.3)	10
	Other		36

The following data are indicated for each group code: land-cover type, the total area in hectares occupied by each type (in parentheses, the percentage of the type area relative to the total surface type area of the study site), and the percentage of correspondence (proportion of all the area covered by a vegetation group that corresponds to a given land-cover type). Only the main types that cover the vegetation groups are included.

3.3. Explanatory Topographic Factors of FAPAR-M Spatial Variability

The SAR model that minimised the value of the AIC incorporated the topographic aspect, slope, height, and the topographic aspect: slope interaction as explanatory factors of FAPAR-M for the main vegetation cover in the study area: evergreen oak forest. The value of the spatial autoregressive parameter in the model $\rho = 0.82$ ($p < 2.22 \times 10^{-16}$) indicated a high spatial autocorrelation of the data. The Lagrange Multiplier Test indicated that the autocorrelation of the residues was not significant (test value = 0.89; $p = 0.34$). Table 4 shows the parameters from the application of the SAR model, with the statistical significance for the model estimates. Figure 14 shows the density scatter-plots between FAPAR-M and the explanatory topographic variables, analysed for the topographic aspects.

Table 4. Parameters from the SAR model.

Parameter	Estimate	Std. Error	z	Pr(> z)
Intercept	1.4281×10^{-1}	1.1382×10^{-2}	12.5473	$<2.2 \times 10^{-16}$
North	-1.4310×10^{-2}	8.0961×10^{-3}	-1.7676	0.0771347
West	-2.5176×10^{-2}	6.5837×10^{-3}	-3.8241	0.0001313
South	1.0092×10^{-2}	8.6294×10^{-3}	1.1695	0.2422015
Slope	-2.9343×10^{-4}	1.0502×10^{-4}	-2.7942	0.0052036
Height	-2.2127×10^{-5}	7.4082×10^{-6}	-2.9868	0.0028187
North: Slope	6.6755×10^{-4}	1.9416×10^{-4}	3.4382	0.0005856
West: Slope	5.6688×10^{-4}	1.5431×10^{-4}	3.6737	0.0002391
South: Slope	-6.4393×10^{-4}	2.1640×10^{-4}	-2.9757	0.0029236

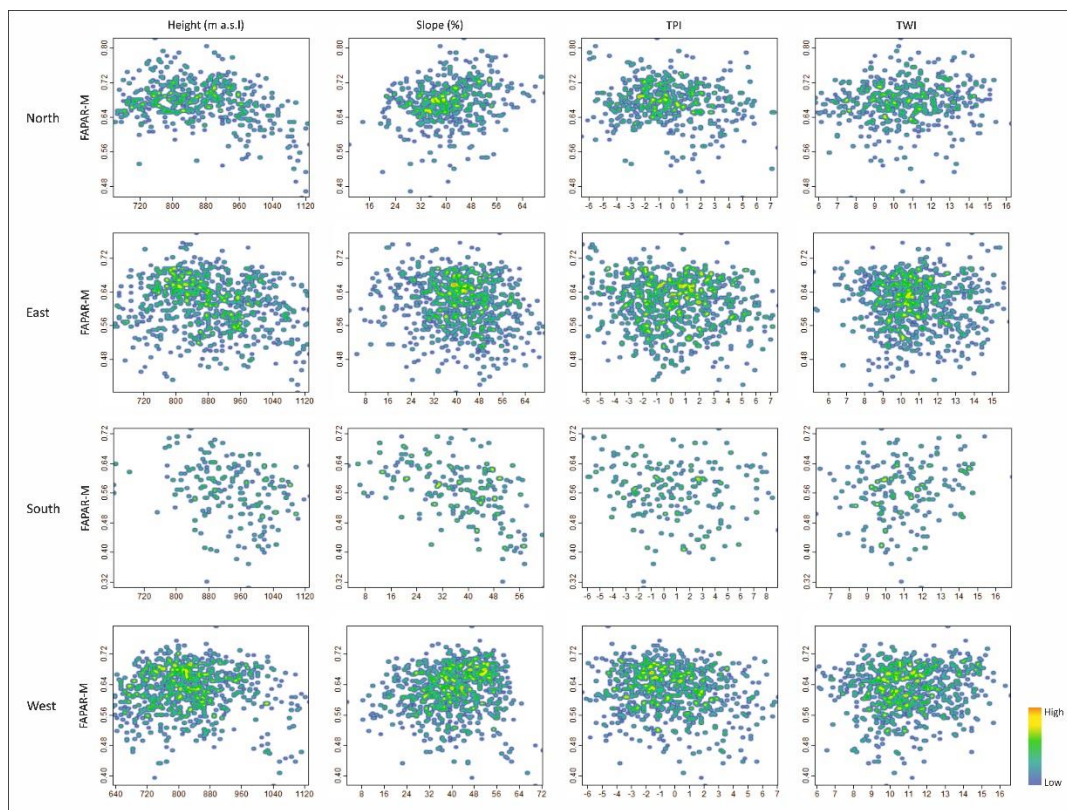


Figure 14. Density scatter-plots between FAPAR-M of the main type of land cover, evergreen oak forest (*Quercus ilex*), and the topographic variables: height (metres above sea level), slope (in percentage), Topographic Wetness Index (TWI) and Topographic Position Index (TPI), analysed for the topographic aspects.

Finally, complementary analyses with general linear models (GLMs) using data from random points obtained by spatial samplings of the images ($n = 200$, minimum distance between points of 100 m to reduce the spatial autocorrelation of the spatial data) also indicated the topographic aspect, slope, height, and the topographic aspect: slope interaction as explanatory factors of FAPAR-M spatial variability, with a coefficient of determination, R^2 , of 0.35 ($p < 7.58 \times 10^{-15}$). The normality and homoscedasticity of the residuals for the complementary GLM model were also visually inspected.

4. Discussion

4.1. Validation of Satellite Products

We defined the study area and geolocated specific coordinates, taking into account the representativeness of natural conditions of Mediterranean forests to minimise anthropic conditions, for facilitating future studies of the relationships between the inter-annual dynamics of the seasonal curves and environmental changes.

The ground measurements represented only a fraction of the range of FAPAR values at the study site due to the difficulty of accessing the terrain. The absence of measurements with low FAPAR values was indirectly countered by the geolocation of the two additional units of bare soil by the visual interpretation of VHR satellite imagery using Google Earth. FAPAR values lower than 0.58 could not be sampled and two bare soil points with FAPAR = 0 were added.

The validation results of the Sentinel-2 FAPAR product for the study site and sampling period agreed well with the ground-truth data. Multi-temporal campaigns may be required to assess the temporal accuracy of the satellite products for the study site, especially for late autumn and early winter, but are not strictly mandatory when validating biophysical products [15].

We highlight the possibility of using the ground-truth database, as derivations of the validation, to validate FAPAR global products, with lower spatial resolution but higher revisit frequency (e.g., PROBA-V and MODIS). Up-scaling ESU ground-measurement techniques (e.g., following the Validation of Land European Remote Sensing Instrument, VALERI guidelines, <http://w3.avignon.inra.fr/valeri/>) could increase the set of remote sensing products validated for the study site, strengthening the possibilities of monitoring these ecosystems at different spatial and temporal scales.

4.2. Analysis and Characterisation of Functional-Trait Dynamics

The characterisation of ecosystems based on functional-trait dynamics derived from remotely sensed data complements structural studies for describing the heterogeneity of ecosystems [1,3]. Several studies have been developed for characterising functional activity of vegetation cover at a regional scale [1,4–9,11]. Most of these studies covered large regional scales, with remote sensors of medium and low spatial resolution (e.g., MODIS and NOAA/AVHRR), where seasonal dynamics were characterised using the NDVI or the Enhanced Vegetation Index (EVI) as proxies of the FAPAR. We applied these approaches and remote-sensing techniques to characterise the functional-traits dynamics of the vegetation cover for a representative area of the Prades Mediterranean ecosystem, at a smaller landscape scale, higher level of detail (10×10 m pixels) and using FAPAR seasonal curves directly. The construction of a temporal data series from the MSI data [14] allowed us to obtain highly detailed information for the FAPAR intra-annual activity over the study site and consequently for the dynamics of potential primary productivity [12], a key aspect of ecosystem functioning [44,45].

The methodology to characterise the functional-trait dynamics of the vegetation cover at high spatial resolution in Prades Mediterranean Forest is objective and repeatable over time using the same set of variables. Each pixel of the remotely sensed data was defined using variables with a clear biological meaning and analysed from their individual seasonal behaviours.

The remotely sensed data used for the construction of the seasonal curves corresponded to the period 2016/2017. The FAPAR dynamics therefore did not correspond to the mean dynamics of the study site but characterised the behaviour of the vegetation activity for that period. Future studies will

be able to characterise the mean curves for each pixel of these ecosystems or will be able to design monitoring protocols to analyse their behaviours over time.

We performed linear interpolations for the late autumn and early winter FAPAR products for constructing the seasonal curves, due to the lack of satellite images, in addition to the detection of contaminated pixels by terrain shadows and the uncertainty of the accuracy of the images for these periods. The low solar angle at the revisit times for Sentinel-2 in these periods generated terrain shadows in areas of steep topographic slopes that could substantially decrease the FAPAR values.

We did not attempt to assimilate the classes of vegetation groups to particular land-cover types, because different types of vegetation covers may have similar FAPAR seasonal dynamics, and the same type may have different patterns of FAPAR annual activity [1]. This internal heterogeneity in each land-cover type can be attributed to the environmental variability of the study area (e.g., soil depth, soil fertility, and water availability) and to the specific species composition in each pixel. The land-cover types used in this study for characterising functional-trait dynamics corresponded to a classification of the main plant species at each site (Appendix A). Pixels with a main forest species mixed with one or more secondary forest species, and the characteristics and dynamics of the understory, can contribute substantially to the heterogeneity of FAPAR dynamics. The FAPAR seasonal curves for each land-cover type may therefore differ from the typical curves expected for a particular plant species, because they characterise ecosystem vegetation activity.

4.3. Explanatory Topographic Factors of FAPAR-M Spatial Variability

The spatial heterogeneity of the FAPAR-M of the main vegetation cover of the study area, evergreen oak forest, was due mainly to the topographic aspect, slope, height, and the topographic aspect: slope interaction. A complementary analysis with GLMs, using data from random points obtained by spatial samplings of the images, also identified topographic aspect, slope, height, and the topographic aspect: slope interaction as the most important explanatory topographic variables of FAPAR-M heterogeneity, explaining 35% of the spatial heterogeneity.

Topographic aspect had the lowest FAPAR-M values in the south-facing slopes and the highest values in the north-facing slopes, as expected due to the higher solar radiation received on the southern orientations at these latitudes, with effects on evapotranspiration and storage of soil moisture. The range of FAPAR-M values, however, was highly dispersed for each aspect. Height and topographic slope, despite being selected in the explanatory SAR models with a weak and negative slope, had highly scattered data points. FAPAR-M decreased greatly with the topographic slope for south-facing slopes, suggesting an increasing soil moisture limiting factor.

The percentage of FAPAR-M variability not accounted for may have been due to other environmental factors not included in the present study, such as soil depth. Soil depth is associated with soil fertility, water availability, and the development of root systems and so could be relevant to the heterogeneity of FAPAR-M in these ecosystems.

The spatial heterogeneity of FAPAR-M was not correlated with TWI or TPI at the study site, contrary to the expected relationship with water availability. The lack of correlation of FAPAR-M with TWI and TPI could be due to diverse factors. First, the ability of TWI and TPI to explain spatial patterns of water availability are limited, because water availability does not depend only on the topography (e.g., it is also influenced by factors such as radiation, physical and chemical properties of the soil, and microrelief conditions not captured by the spatial resolution of the DEM [46,47]). Second, we used a predefined TPI landscape unit of 150 m to highlight minor valleys and ridges and used the MFD-md algorithm, because it had the best significant, albeit low, correlation with the data for in situ soil moisture in a study conducted in a mountainous system in Poland [25], but it is highlighted that the TPI landscape units considered, or the TWI flow algorithms selected, could generate different results [25,48–50].

The spatial autocorrelation of the data was not completely eliminated, despite resampling the dependent and independent variables to cells of lower spatial resolution. An increase in the size of the cells per unit area could help to reduce the spatial autocorrelation of the data, but with the potential loss of detail in the relationships between FAPAR-M and the topographic variables.

We aimed to characterise the relationships between the annual activity of FAPAR (though FAPAR-M) and topographic variables. The intra-annual temporal variation of the spatial heterogeneity and the specific relationships between FAPAR and the topographic factors for each semi-season were not analysed in this study. Incorporating specific analyses for each semi-season could improve the characterisation of functional-trait dynamics and our understanding of the explanatory factors of the FAPAR heterogeneity through the year.

5. Conclusions

This study is the first to characterise the spatial heterogeneity of the intra-annual dynamics of the fraction of the photosynthetically active radiation absorbed by the vegetation canopy for a portion of a Mediterranean forest in Prades, Tarragona, using high-spatial-resolution data from the Sentinel-2 satellite. The methodology used was objective and repeatable over time using the same set of variables to enable comparisons with future characterisations.

We validated the FAPAR satellite products with ground-truth data for the period of maximum greenness of the vegetation, with very good agreement (RMSE of 0.03 FAPAR). Conducting multi-temporal field campaigns, however, would be appropriate to ensure the seasonal stability of the satellite products given the characteristics of the topographic slopes on the study area, mainly for periods characterised by terrain shadows due to lower solar angles that could substantially decrease the FAPAR values. Alternative methodologies to the DHP should be explored for these periods, due to the potential higher interference of non-green elements in the digital images.

Slope, height, and the topographic aspect: slope interaction accounted for most of the heterogeneity of FAPAR-M for the main vegetation cover. Some of the heterogeneity not accounted for may have been due to other topographic factors not included in the study, such as soil depth. We recommend that incorporating soil depth into the models could be relevant for improving our understanding of the explanatory factors of the spatial heterogeneity of the annual magnitude of the absorption of photosynthetically active radiation by the vegetation canopy for these ecosystems.

Author Contributions: S.S. and A.V. conceived the research approach and designed the experiment with contributions from I.F. and J.P. The data was collected and processed by S.S. and A.V., S.S., A.V., I.F. and J.P. contributed to the analysis and discussion of results. The manuscript was written by S.S. with contributions from A.V., I.F. and J.P.

Funding: This research was funded by the EC Copernicus Global Land Service (CGLOPS-1, 199494-JRC), the European Research Council Synergy grant ERC-SyG-2013-610028 IMBALANCE-P, the Spanish Government grant CGL2016-79835-P and the Catalan Government grant SGR 2017-1005.

Acknowledgments: We thank Francesco Vuolo and Mateusz Żóltak for their technical assistance with EODC data service platform for Sentinel-2 products, Marie Weiss for her support with CAN-EYE, Fernando Camacho for his guidance on FAPAR product validation, Germán Baldi for his valuable comments in different stages of the study, Kevin Bórnez and Adrià Descals for their participation in the field campaign collecting ground data, and Aldana Persia for her collaboration in the graphical design. SS acknowledges the support from the Argentina BEC.AR Scholarship Programme.

Conflicts of Interest: The authors declare no conflict of interest.

Appendix A

Table A1. Description of the categories of the land-cover map of Catalonia [21] (level 5 of the legend) for the study site.

Land-Cover Type (Canopy Coverage)	Description
Evergreen oak forest ($\geq 20\%$)	Natural forests with a tree canopy consisting mainly of <i>Quercus ilex</i> (evergreen oak) with a tree density $>20\%$.
Scots pine forest ($\geq 20\%$)	Natural forests with a tree canopy consisting mainly of <i>Pinus sylvestris</i> (Scots pine) with a tree density $>20\%$.
Austrian pine forest ($\geq 20\%$)	Natural forests with a tree canopy consisting mainly of <i>Pinus nigra</i> (Austrian pine) with a tree density $>20\%$.
Pubescent oak forest ($\geq 20\%$)	Natural forests with a tree canopy consisting mainly of <i>Quercus pubescens</i> (Pubescent oak) with a tree density $>20\%$.
Evergreen oak forest (5–20%)	Natural forests with a tree canopy consisting mainly of <i>Quercus ilex</i> (evergreen oak) with a tree density of 5–20%.
Scree	Surface where boulders and sharp pebbles have accumulated on the flanks of a mountain. The area is dry with sparse vegetation.
Shrubland	Formations with a substantial covering of shrubs or shrubby trees, when tree cover is $<5\%$.
Maritime pine forest ($\geq 20\%$)	Natural forests with a tree canopy consisting mainly of <i>Pinus pinaster</i> (maritime pine) with a tree density $>20\%$.
Pyrenean oak forest ($\geq 20\%$)	Natural forests with a tree canopy consisting mainly of <i>Quercus pyrenaica</i> (Pyrenean oak) with a tree density $>20\%$.
Other deciduous trees ($\geq 20\%$)	Natural forests with a tree canopy consisting mainly of deciduous trees (e.g., northern red oak, maple, nettle tree) with a tree density $>20\%$.
Spanish chestnut forest ($\geq 20\%$)	Natural forests with a tree canopy consisting mainly of <i>Castanea sativa</i> (Spanish chestnut) with a tree density $>20\%$.

Appendix B

Table A2. Geolocation details in the WGS84 geographic coordinate system and FAPAR values for each elementary sampling unit.

ESU #	Latitude	Longitude	Land-Cover Type (Canopy Coverage)	Number of DHP	FAPAR
1	41°20'7.9"	1°0'48.8"	Scots pine forest ($\geq 20\%$)	18	0.629
2	41°20'09"	1°0'48.4"	Scots pine forest ($\geq 20\%$)	9	0.65
3	41°20'18.5"	1°01'03.4"	Evergreen oak forest ($\geq 20\%$)	10	0.675
4	41°20'17.3"	1°01' 11"	Evergreen oak forest ($\geq 20\%$)	17	0.63
5	41°20'18.8"	1°01'10.0"	Evergreen oak forest ($\geq 20\%$)	10	0.675
6	41°20'19.7"	1°01'09.8"	Evergreen oak forest ($\geq 20\%$)	10	0.635
7	41°20'21.11"	1°01'09"	Scots pine forest ($\geq 20\%$)	11	0.645
8	41°20'20.4"	1°01'10.7"	Evergreen oak forest ($\geq 20\%$)	10	0.646
9	41°20'30"	1°01'28.5"	Evergreen oak forest ($\geq 20\%$)	11	0.65
10	41°20'29.4"	1°01'26.8"	Evergreen oak forest ($\geq 20\%$)	11	0.665
11	41°20'30"	1°01'25.7"	Evergreen oak forest ($\geq 20\%$)	8	0.64
12	41°20'38.8"	1°02'00"	Evergreen oak forest ($\geq 20\%$)	10	0.62
13	41°20'46"	1°02'03.3"	Evergreen oak forest ($\geq 20\%$)	11	0.674
14	41°20'19.6"	1°01'50.8"	Evergreen oak forest ($\geq 20\%$)	11	0.665
15	41°20'19.7"	1°01'49.8"	Evergreen oak forest ($\geq 20\%$)	12	0.655
16	41°20'22.5"	1°02'49.3"	Maritime pine forest	10	0.635
17	41°20'23.1"	1°02'49.9"	Maritime pine forest	10	0.67
18	41°20'26.2"	1°02'55.9"	Maritime pine forest	10	0.58
19	41°19'53.2"	1°02'40.9"	Spanish chestnut forest ($\geq 20\%$)	11	0.906
20	41°19'50.8"	1°02'37.5"	Spanish chestnut forest ($\geq 20\%$)	11	0.832
21	41°19'45"	1°02'56.8"	Scots pine forest ($\geq 20\%$)	11	0.62
22	41°19'43.3"	1°02'56.7"	Scots pine forest ($\geq 20\%$)	11	0.67
23	41°19'39.2"	1°02'28.1"	Pyrenean oak forest ($\geq 20\%$)	11	0.891
24	41°19'37.3"	1°02'27.4"	Pyrenean oak forest ($\geq 20\%$)	12	0.883
25	41°19'46.1"	1°02'37.1"	Evergreen oak forest ($\geq 20\%$)	14	0.732
26	41°19'48.8"	1°02'33"	Evergreen oak forest ($\geq 20\%$)	12	0.738
27	41°19'49.1"	1°02'28.8"	Evergreen oak forest ($\geq 20\%$)	11	0.771
28	41°20'28.2"	1°03'22.1"	Pubescent oak forest ($\geq 20\%$)	14	0.79
29	41°20'12.28"	1°2'28.58"	Bare soil	0	0
30	41°19'29.65"	1°2'36.26"	Bare soil	0	0

The following data are indicated for each elementary sampling unit (ESU): latitude and longitude coordinates in the WGS84 Geographic Coordinate System, the type of land cover (percent canopy coverage), the number of digital hemispherical photographs (DHP) acquired, and the ground-truth values of the fraction of absorbed photosynthetically active radiation (FAPAR) obtained. ESUs 29 and 30 correspond to the extra units of bare soil obtained from very-high-resolution satellite imagery.

Appendix C

Table A3. Collinearity analysis of the explanatory topographic factors. The Pearson correlation coefficients and the generalised variance-inflation factors (GVIFs) did not suggest the elimination of variables.

Correlation matrix (Pearson's *r*).

	Slope	TWI	TPI	Height
Slope	1	−0.04	0.08	0.23
TWI	−0.04	1	−0.4	−0.08
TPI	0.08	−0.4	1	0.3
Height	0.23	−0.08	0.3	1

The criterion for a strong Pearson correlation was 0.7.

Generalised variance-inflation factors.

	GVIF
Slope	1.08
TWI	1.2
TPI	1.31
Height	1.26
Aspect	1.14

The criterion for collinearity was a GVIF ≥ 5 .

References

1. Paruelo, J.M.; Jobbágy, E.G.; Sala, O.E. Current distribution of ecosystem functional types in temperate South America. *Ecosystems* **2001**, *4*, 683–698. [[CrossRef](#)]
2. Myneni, R.B.; Keeling, C.D.; Tucker, C.J.; Asrar, G.; Nemani, R.R. Increased plant growth in the northern high latitudes from 1981 to 1991. *Nature* **1997**, *386*, 698. [[CrossRef](#)]
3. Paruelo, J.M. La caracterización funcional de ecosistemas mediante sensores remotos. *Ecosistemas* **2008**, *17*, 22.
4. Alcaraz, D.; Paruelo, J.; Cabello, J. Identification of current ecosystem functional types in the Iberian peninsula. *Global Ecol. Biogeogr.* **2006**, *15*, 200–212. [[CrossRef](#)]
5. Baldi, G.; Noretto, M.D.; Aragon, R.; Aversa, F.; Paruelo, J.M.; Jobbágy, E.G. Long-term satellite NDVI data sets: Evaluating their ability to detect ecosystem functional changes in South America. *Sensors* **2008**, *8*, 5397–5425. [[CrossRef](#)] [[PubMed](#)]
6. Lara, B.; Gandini, M.; Gantes, P.; Matteucci, S.D. Regional patterns of ecosystem functional diversity in the Argentina pampas using MODIS time-series. *Ecol. Inform.* **2018**, *43*, 65–72. [[CrossRef](#)]
7. Soriano, A.; Paruelo, J.M. Biozones: Vegetation units defined by functional characters identifiable with the aid of satellite sensor images. *Global Ecol. Biogeogr. Lett.* **1992**, *2*, 82–89. [[CrossRef](#)]
8. Baeza, S.; Paruelo, J.M.; Altesor, A. Functional characterization of Uruguayan vegetation using remote sensing. *Interciencia* **2006**, *31*, 382–388.
9. Cabello, J.; Alcaraz-Segura, D.; Reyes Díez, A.; Lourenço, P.; Requena-Mullor, J.; Bonache, J.; Castillo, P.; Valencia, S.; Naya, J.; Ramírez, L.; et al. Sistema para el seguimiento del funcionamiento de ecosistemas en la red de parques nacionales de España mediante teledetección. *Rev. Teledetec.* **2016**, *46*, 119–131. [[CrossRef](#)]
10. Pettorelli, N.; Vik, J.O.; Mysterud, A.; Gaillard, J.M.; Tucker, C.J.; Stenseth, N.C. Using the satellite-derived NDVI to assess ecological responses to environmental change. *Trends Ecol. Evol.* **2005**, *20*, 503–510. [[CrossRef](#)] [[PubMed](#)]
11. Alcaraz-Segura, D.; Paruelo, M.J.; Epstein, E.H.; Cabello, J. Environmental and human controls of ecosystem functional diversity in temperate South America. *Remote Sens.* **2013**, *5*, 127–154. [[CrossRef](#)]
12. Monteith, J.L. Climate and the efficiency of crop production in Britain. *Philos. Trans. R. Soc. Lond.* **1977**, *281*, 277–294. [[CrossRef](#)]

13. Global Climate Observing System (GCOS). *Systematic Observation Requirements for Satellite-Based Products for Climate-2011 Update: Supplemental details to the satellite-based component of the "Implementation Plan for the Global Observing System for Climate in Support of the UNFCCC (2010 update)"*; World Meteorological Organization: Geneva, Switzerland, 2011; p. 138.
14. Vuolo, F.; Žóltak, M.; Pipitone, C.; Zappa, L.; Wenng, H.; Immitzer, M.; Weiss, M.; Baret, F.; Atzberger, C. Data service platform for Sentinel-2 surface reflectance and value-added products: System use and examples. *Remote Sens.* **2016**, *8*, 938. [[CrossRef](#)]
15. Camacho, F.; Baret, F.; Lacaze, R. Guidelines for field campaigns, issue I1.10. Available online: <http://fp7-imagines.eu/pages/documents.php> (accessed on 7 August 2018).
16. Latorre-Sánchez, C.; Camacho, F.; Mattar, C.; Santamaría-Artigas, A.; Leiva-Büchi, N.; Lacaze, R. LAI, FAPAR and FCOVER ground-truth map creation from FASAT-C satellite imagery and in-situ measurements in Chimbarongo, Chile, for satellite products validation. *Rev. Teledetec.* **2016**, *47*, 51–64. [[CrossRef](#)]
17. Morisette, J.T.; Baret, F.; Privette, J.L.; Myneni, R.B.; Nickeson, J.E.; Garrigues, S.; Shabanov, N.V.; Weiss, M.; Fernandes, R.A.; Leblanc, S.G.; et al. Validation of global moderate-resolution LAI products: A framework proposed within the CEOS Land Product Validation Subgroup. *IEEE Trans. Geosci. Remote Sens.* **2006**, *44*, 1804–1817. [[CrossRef](#)]
18. Camacho, F.; Lacaze, R.; Latorre, C.; Baret, F.; De la Cruz, F.; Demarez, V.; Di Bella, C.; Fang, H.; García-Haro, J.; Gonzalez, M.P.; et al. A network of sites for ground biophysical measurements in support of Copernicus Global Land Product Validation. In In Proceedings of the IV RAQRS Conference, Torrent, Spain, 22–26 September 2014.
19. GEU. Global Ecology Unit (CREAF-CSIC-UAB) research experimental sites. Available online: http://globalecology.creaf.cat/?page_id=17 (accessed on 7 August 2018).
20. State Meteorological Agency (AEMET), Spanish Government. Available online: <http://www.aemet.es> (accessed on 4 December 2017).
21. Centre for Ecological Research and Forestry Applications (CREAF). Mapa de Cobertes del Sòl de Catalunya (MCSC). Available online: <http://www.creaf.uab.cat/mcsc/> (accessed on 7 August 2018).
22. Baret, F.; Weiss, M.; Bicheron, P.; Berthelot, B. *Sentinel-2 MSI Products-wp1152 Algorithm Theoretical Basis Document for Product Group B*; INRA-EMMAH: Avignon, France, 2010.
23. Beven, K.J.; Kirkby, M.J. A physically based, variable contributing area model of basin hydrology. *Hydrol. Sci. J.* **1979**, *24*, 43–69. [[CrossRef](#)]
24. Qin, C.-Z.; Zhu, A.X.; Pei, T.; Li, B.-L.; Scholten, T.; Behrens, T.; Zhou, C.-H. An approach to computing Topographic Wetness Index based on maximum downslope gradient. *Precis. Agric.* **2011**, *12*, 32–43. [[CrossRef](#)]
25. Raduła, M.W.; Szymura, T.H.; Szymura, M. Topographic Wetness Index explains soil moisture better than bioindication with Ellenberg's Indicator Values. *Ecol. Indicators* **2018**, *85*, 172–179. [[CrossRef](#)]
26. Wilson, J.; Gallant, J. *Terrain Analysis: Principles and Applications*; Wiley: New York, NY, USA, 2000; p. 520. ISBN 978-0-471-32188-0.
27. Weiss, A.D. Topographic position and landforms analysis. Poster presentation, ESRI users conference, San Diego, CA. Available online: http://www.jennessent.com/downloads/tpi-poster-tnc_18x22.pdf (accessed on 21 August 2018).
28. Martínez, B.; García-Haro, F.J.; Camacho-de Coca, F. Derivation of high-resolution Leaf Area Index maps in support of validation activities: Application to the cropland Barrax site. *Agric. For. Meteorol.* **2009**, *149*, 130–145. [[CrossRef](#)]
29. Weiss, M.; Baret, F.; Smith, G.J.; Jonckheere, I.; Coppin, P. Review of methods for in situ Leaf Area Index (LAI) determination: Part II. Estimation of LAI, errors and sampling. *Agric. For. Meteorol.* **2004**, *121*, 37–53. [[CrossRef](#)]
30. Nestola, E.; Sánchez-Zapero, J.; Latorre, C.; Mazzenga, F.; Matteucci, G.; Calfapietra, C.; Camacho, F. Validation of PROBA-V GEOV1 and MODIS C5 & C6 FAPAR products in a deciduous beech forest site in Italy. *Remote Sens.* **2017**, *9*, 126. [[CrossRef](#)]
31. Campos-Taberner, M.; García-Haro, J.F.; Confalonieri, R.; Martínez, B.; Moreno, Á.; Sánchez-Ruiz, S.; Gilabert, A.M.; Camacho, F.; Boschetti, M.; Busetto, L. Multitemporal monitoring of Plant Area Index in the Valencia rice district with PocketLAI. *Remote Sens.* **2016**, *8*, 202. [[CrossRef](#)]

32. Jonckheere, I.; Fleck, S.; Nackaerts, K.; Muys, B.; Coppin, P.; Weiss, M.; Baret, F. Review of methods for in situ Leaf Area Index determination: Part I. Theories, sensors and hemispherical photography. *Agric. For. Meteorol.* **2004**, *121*, 19–35. [[CrossRef](#)]
33. Weiss, M.; Baret, F. *CAN-EYE V6.313 User Manual*; INRA: Avignon, France, 2017.
34. Weiss, M.; Baret, F. CAN-EYE Output Variables. Definitions and Theoretical Background. Available online: <https://www6.paca.inra.fr/can-eye/Documentation/Documentation> (accessed on 15 August 2018).
35. Camacho, F. Standards for in Situ LAI and Biophysical Variables Measurements. JECAM/GEOGLAM. Science meeting Brussels, Belgium 16–17 November. Available online: http://www.jecam.org/A11_JECAM_standard_guidelines_for_in-situ_LAI_collection.pdf (accessed on 7 August 2018).
36. Widlowski, J.-L. On the bias of instantaneous FAPAR estimates in open-canopy forests. *Agric. For. Meteorol.* **2010**, *150*, 1501–1522. [[CrossRef](#)]
37. Piñeiro, G.; Perelman, S.; Guerschman, J.P.; Paruelo, J.M. How to evaluate models: Observed vs. Predicted or Predicted vs. Observed? *Ecol. Model.* **2008**, *216*, 316–322. [[CrossRef](#)]
38. Belsley, D.; Kuh, E.Q.; Welsch, R.E. *Regression Diagnostics: Identifying Influential Data and Sources of Collinearity*; John Wiley & Son: Hoboken, NJ, USA, 1980; p. 292.
39. James, G.; Witten, D.; Hastie, T.; Tibshirani, R. *An introduction to statistical learning: With applications in R*; Springer-Verlag: New York, NY, USA, 2013; p. 426.
40. Fox, J.; Weisberg, S.; Price, B.; Adler, D.; Bates, D.; Baud-Bovy, G.; Bolker, B.; Ellison, S.; Firth, D.; Friendly, M.; et al. Companion to applied regression. Available online: <https://cran.r-project.org/web/packages/car/car.pdf> (accessed on 22 August 2018).
41. Bivand, R.; Altman, M.; Anselin, L.; Assunção, R.; Berke, O.; Bernat, A.; Blanchet, G.; Blankmeyer, E.; Carvalho, M.; Christensen, B.; et al. Spatial dependence: Weighting schemes, statistics and models. Available online: <https://cran.r-project.org/web/packages/spdep/spdep.pdf> (accessed on 22 August 2018).
42. Sarmiento-Barbieri, I. An introduction to Spatial Econometrics in R. University of Illinois. Available online: http://www.econ.uiuc.edu/~lab/workshop/Spatial_in_R.html (accessed on 7 August 2018).
43. Akaike, H. A new look at the statistical model identification. *IEEE Trans. Automat. Contr.* **1974**, *19*, 716–723. [[CrossRef](#)]
44. McNaughton, S.J.; Oesterheld, M.; Frank, D.A.; Williams, K.J. Ecosystem-level patterns of primary productivity and herbivory in terrestrial habitats. *Nature* **1989**, *341*, 142. [[CrossRef](#)] [[PubMed](#)]
45. Odum, E.P. *Fundamentals of Ecology*; Saunders: Philadelphia, PA, USA, 1953; p. 384.
46. Zhu, Q.; Lin, H. Influences of soil, terrain, and crop growth on soil moisture variation from transect to farm scales. *Geoderma* **2011**, *163*, 45–54. [[CrossRef](#)]
47. Moeslund, J.E.; Arge, L.; Bøcher, P.K.; Dalgaard, T.; Ejrnæs, R.; Odgaard, M.V.; Svenning, J.-C. Topographically controlled soil moisture drives plant diversity patterns within grasslands. *Biodivers. Conserv.* **2013**, *22*, 2151–2166. [[CrossRef](#)]
48. Zhou, Q.; Liu, X. Error assessment of grid-based flow routing algorithms used in hydrological models. *Int. J. Geogr. Inf. Sci.* **2002**, *16*, 819–842. [[CrossRef](#)]
49. Schmidt, F.; Persson, A. Comparison of DEM data capture and Topographic Wetness Indices. *Precis. Agric.* **2003**, *4*, 179–192. [[CrossRef](#)]
50. Wilson, J. Digital terrain modeling. *Geomorphology* **2012**, *137*, 107–121. [[CrossRef](#)]

